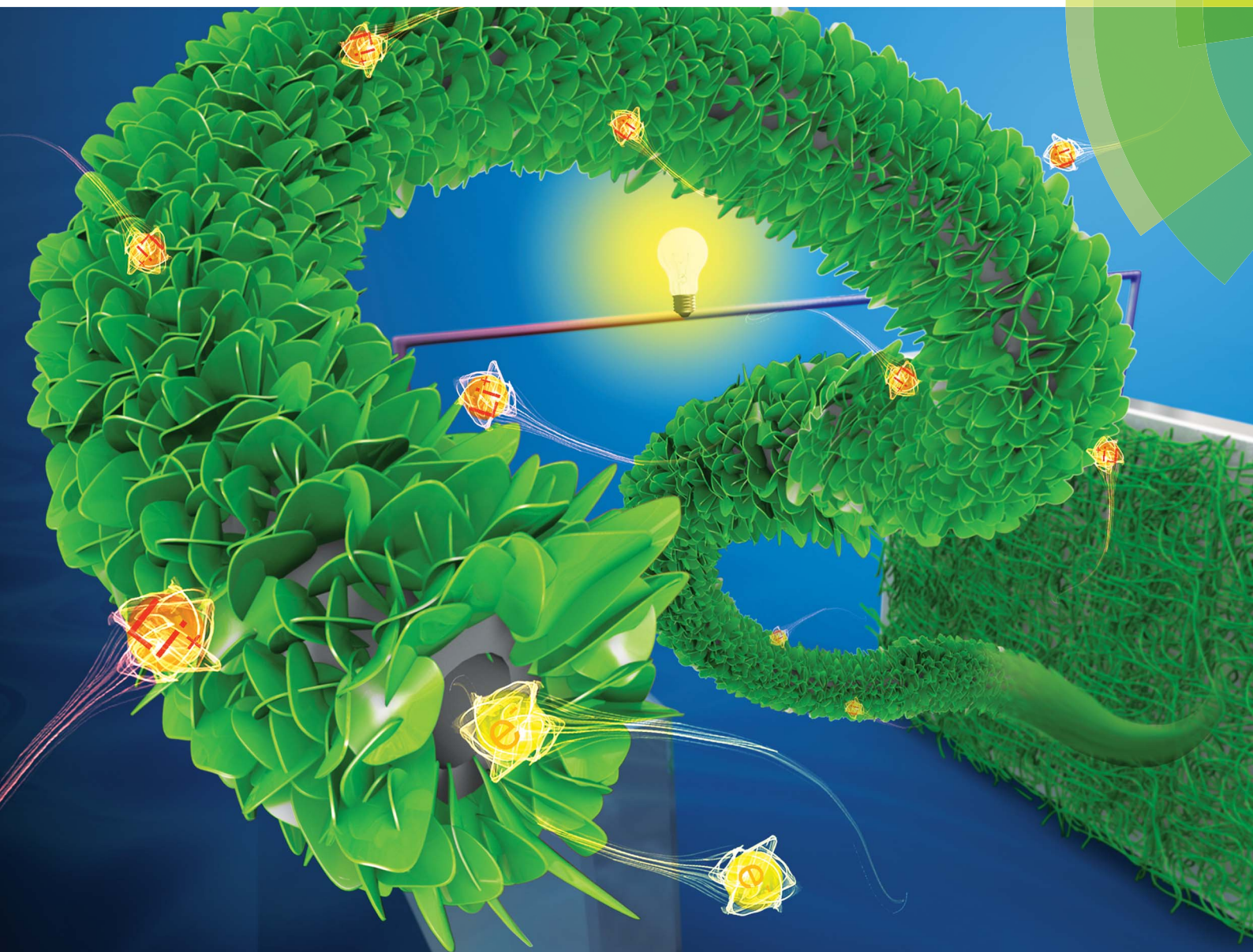


Journal of Materials Chemistry A

Materials for energy and sustainability

rsc.li/materials-a



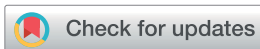
ISSN 2050-7488



PAPER

An-Hui Lu *et al.*

Ultrathin phyllosilicate nanosheets as anode materials with superior rate performance for lithium ion batteries

Cite this: *J. Mater. Chem. A*, 2018, **6**,
1397

Ultrathin phyllosilicate nanosheets as anode materials with superior rate performance for lithium ion batteries†

Xiang-Qian Zhang,^a Wen-Cui Li,^a Bin He,^a Dong Yan,^a Shuang Xu,^a
Yuliang Cao^b and An-Hui Lu^{b*}

Phyllosilicates with SiO₄ tetrahedra and metal cation-containing octahedrally composed sheet structures are promising anode materials for lithium-ion batteries, as they have high abundance and three times the theoretical capacity of graphite. The main challenges associated with the phyllosilicate anode are the structural degradation and the low rate capability caused by the low intrinsic electrical conductivity and the large strain upon cycling. Herein, we develop hybrid architectures by *in situ* inlaying nickel phyllosilicate within tubular carbon frameworks to form ultrathin phyllosilicate nanosheets, where the phyllosilicate is spatially incorporated within carbon rather than superficially coating on the outer surface. The carbon framework significantly enhances the electrical conductivity and steadily buffers volumetric strain of the ultrathin phyllosilicate nanosheets upon cycling. The tubular hybrid architectures can provide accessible electroactive sites and allow rapid electron/ion transfer. When applied as lithium-ion battery anode materials, the prepared hierarchical nickel phyllosilicate/carbon hybrids deliver an exceptional rate capability (1017 mA h g⁻¹ at 0.2 A g⁻¹ and 540 mA h g⁻¹ at 2.0 A g⁻¹) and good cycling stability (585 mA h g⁻¹ after 200 cycles at 1.0 A g⁻¹), and outperform the previously reported nickel silicate materials. A full cell constructed with the nickel phyllosilicate anode and a commercial LiNi_{1/3}Co_{1/3}Mn_{1/3}O₂ cathode exhibits high reversible capacity in the voltage range of 0.2–4.0 V, demonstrating the great potential of phyllosilicates as anode materials.

Received 6th October 2017
Accepted 12th November 2017

DOI: 10.1039/c7ta08817e

rsc.li/materials-a

1. Introduction

Exploiting high capacity anode materials is one of the most effective ways to construct high energy density lithium-ion batteries (LIBs) for large-scale applications such as electric vehicles and electric grids.^{1–4} Transition metal phyllosilicates have a layered structure formed by sheets of tetrahedral silicon-oxygen (SiO₄) and sheets of octahedral metal cations. This makes these materials excellent candidates for the anodes of LIBs as they can facilitate reversible lithium insertion and extraction, and contribute high theoretical capacities with multi-electron transfer reactions (*e.g.*, 1107 mA h g⁻¹ for nickel phyllosilicate).^{5–9} Nevertheless, the low electrical conductivity and the large strain upon cycling of bulk metal phyllosilicates unavoidably cause low rate capability and fast capacity decay.^{10–13}

Scaling down the characteristic dimensions of the bulk phyllosilicates to the nanometer scale and incorporating them in conductive carbon frameworks to form hybrids is an effective solution to overcome the aforementioned obstacles.^{14–17} For example, a CNT/nickel silicate hybrid has been prepared by growing silicate nanosheets on the outer surface of oxidized CNTs through C–O–Si covalent bonding.¹⁸ The one-dimensional hollow structure and good electron transfer ability of CNTs can theoretically relax the strain upon cycling and better the conductivity of phyllosilicates. However, such C–O–Si covalent bonded carbon/silicate structures cannot properly ensure efficient electrical contact and structural integrity at the interfaces between the two disparate components.^{19,20} As a result, the enhancement in conductivity of the metal silicates is limited. It is not hard to imagine that stripping of the silicate nanosheets will inevitably happen after a long repeated lithium insertion/extraction process, giving rise to unfavorable rate performance and capacity degradation. For graphene modified phyllosilicates, similar problems occurred because graphene oxide was always used as the first option to bond or assemble other components through surface electric charge or functional groups.^{21–23} These considerations have motivated the investigation of a better method for the preparation of carbon-modified phyllosilicate anode materials.²⁴

^aSchool of Chemical Engineering, State Key Laboratory of Fine Chemicals, Dalian University of Technology, Dalian 116024, P. R. China. E-mail: anhuilu@dlut.edu.cn

^bHubei Key Laboratory of Electrochemical Power Sources, College of Chemistry and Molecular Sciences, Wuhan University, Wuhan, Hubei 430072, P. R. China

† Electronic supplementary information (ESI) available: SEM images of NSF, CV curves and GC profiles of NSF anodes, SEM images of CNSF after cycling tests, etc. See DOI: 10.1039/c7ta08817e

As a response to this challenge, herein, we propose a facile and mild strategy for the preparation of ultrathin nickel phyllosilicate nanosheets inlaid into carbon frameworks, like plants growing from the soil. In our case, tubular mesoporous carbon/silica nanocomposites were used as starting substrates, and nickel nitrate was used as a metal precursor. By virtue of its highly dispersed features, nanosized silica in the substrate was transformed *in situ* into ultrathin nickel phyllosilicate nanosheets in the confined mesopore space under mild hydrothermal conditions. The integrated carbon framework plays an important role as a physical buffer in enhancing the electrical conductivity and cycling durability by confining and stabilizing the phyllosilicate nanosheets. Impressively, the nickel phyllosilicate/carbon hybrid anodes deliver high performance in LIBs, and outperform the previously reported nickel silicate materials. This approach paves the way for the synthesis of other metal silicates with stable electrochemical performance.

2. Experimental section

2.1 Chemicals

All of the following chemicals were used as received without further purification. Ammonium hydroxide ($\text{NH}_3 \cdot \text{H}_2\text{O}$, 28%), nickel nitrate hexahydrate ($\text{Ni}(\text{NO}_3)_2 \cdot 6\text{H}_2\text{O}$), copper nitrate hydrate ($\text{Cu}(\text{NO}_3)_2 \cdot 3\text{H}_2\text{O}$), manganese chloride tetrahydrate ($\text{MnCl}_2 \cdot 4\text{H}_2\text{O}$), and ammonium chloride (NH_4Cl) were supplied by Sinopharm Chemical Reagent Co. (China).

2.2 Synthesis of the carbon-incorporated nickel silicate composite (CNSF) and bare nickel silicate (NSF)

The tubular mesoporous carbon/silica composite starting substrates were synthesized according to our previous work.²⁵ Then, the carbon/silica composite (154 mg) and nickel nitrate hexahydrate (2.5 mmol) were dissolved in deionized water. Then, ammonium chloride (20 mmol) and $\text{NH}_3 \cdot \text{H}_2\text{O}$ (2 mL) dissolved in deionized water were added. After stirring for five minutes, the solution was transferred into a 150 mL autoclave and maintained at 90 °C for 10 h. The product was centrifuged and washed with deionized water and ethanol before drying at 50 °C for 12 h. For the synthesis of bare NSF, the black carbon/silica composite was first heated in a muffle furnace at 500 °C for 5 h to burn off the carbon component and thus obtain white hollow silica fibers. The rest of the synthesis route for NSF is identical to that of CNSF.

2.3 Synthesis of carbon-incorporated manganese silicate fibers (CMnSF) and copper silicate fibers (CCuSF)

The experimental conditions for the synthesis of CMnSF and CCuSF are similar to those of CNSF, except for the replacement of Ni^{2+} with Mn^{2+} and Cu^{2+} and reaction at 140 °C for 10 h and 6 h, respectively.

2.4 Characterization

Powder X-ray diffraction (XRD) measurements were made on a Rigaku D/Max 2400 diffractometer using $\text{Cu K}\alpha$ radiation ($\lambda = 0.15406$ nm). Nitrogen sorption isotherms were measured with

a Micromeritics TriStar 3000 adsorption analyzer. The specific surface area was calculated from the adsorption data in the relative pressure range from 0.05 to 0.3 using the Brunauer–Emmett–Teller (BET) method. Scanning electron microscopy (SEM) investigations and energy-dispersive X-ray spectroscopy (EDS) were carried out with a FEI Nova NanoSEM 450 instrument. Transmission electron microscope (TEM) images and high-resolution TEM (HR-TEM) and high-angle annular dark-field scanning TEM (HAADF-STEM) images were collected on a FEI Tecnai F30 instrument with an element energy-dispersive X-ray spectrometer (EDS). Thermogravimetric analysis was conducted on a NETZSCH STA 449 F3 thermogravimetric analyzer under a nitrogen flow. X-ray photoelectron spectroscopy (XPS) data were obtained with an ESCALAB250 electron spectrometer.

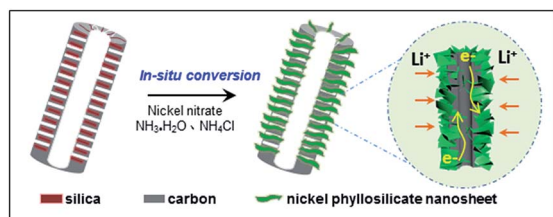
2.5 Electrochemical measurements

CNSF electrodes were fabricated using a mixture of 70 wt% active material, 20 wt% conductive carbon black and 10 wt% binder. The mass loading of the active materials in the electrodes is about 1 mg cm^{-2} . Electrochemical tests were performed using CR2025 coin-type cells assembled in an argon-filled glovebox, using Li metal as the counter electrode and a Celgard 2400 membrane as the separator. The electrolyte consisted of a solution of 1 M LiPF_6 in dimethyl carbonate (DMC), ethyl methyl carbonate (EMC) and ethylene carbonate (EC). Unless otherwise stated, the capacity of CNSF in the half-cell test is calculated based on the total weight of the composite. Galvanostatic charge and discharge experiments were performed in the range 0.01–3.0 V at room temperature on a Land CT2001A battery test system. Cyclic voltammetry (CV) and electrochemical impedance spectroscopy (EIS) measurements were carried out on an electrochemical workstation (CHI660D).

Lithium full batteries, using nickel silicate as the anode and commercial $\text{LiNi}_{1/3}\text{Co}_{1/3}\text{Mn}_{1/3}\text{O}_2$ (LiNCM) as the cathode, were assembled. A similar strategy was applied to prepare the cathode: commercial LiNCM was mixed with carbon black and LA133 in the weight ratio of 80 : 10 : 10. The electrolyte and separator used were the aforementioned ones. The weight ratio of cathode to anode was around 6 : 1 to match the capacity. The galvanostatic charge/discharge method was applied to measure the electrochemical performances between 0.2 V and 4.0 V at current densities of 0.1 A g^{-1} based on the anode materials. The anode materials were firstly pre-activated in a half cell to form a stable SEI layer and then taken out for the LIB full cell. The cathodes were directly applied without a pre-activation process.

3. Results and discussion

The synthesis procedure of the ultrathin nickel phyllosilicate nanosheets inlaid into the tubular carbon framework is schematically illustrated in Scheme 1. A tubular mesoporous carbon/silica composite, in which the silica and carbon are highly dispersed at the nanoscale throughout the shell, was used as the starting substrate. Nickel nitrate was then introduced into the substrate and reacted with the highly dispersed



Scheme 1 Schematic illustration for the synthesis of ultrathin nickel phyllosilicate nanosheets inlaid into the tubular carbon framework.

silica in the carbon/silica composite with the help of ammonium hydroxide and ammonium chloride, resulting in the production of ultrathin phyllosilicate nanosheets inlaid into the carbon framework (denoted as CNSF).

The SEM and TEM images in Fig. 1a show that the carbon/silica composite substrates have a 1D tubular structure and a smooth surface. The STEM image and linear EDX element distributions (Fig. S1†) reveal that the silica is spatially interlaced with carbon. N_2 adsorption-desorption analysis (Fig. S1b†) indicates that the carbon/silica composite features a hierarchical micro-mesopore system with a high surface area (S_{BET}) of $952 \text{ m}^2 \text{ g}^{-1}$ and V_{total} of $0.85 \text{ cm}^3 \text{ g}^{-1}$, which are favorable for the rapid diffusion and *in situ* reaction of metal ions with silica. The SEM image (Fig. 1b) indicates that the CNSF products preserve the analogical 1D morphology but exhibit rough and corrugated surfaces. The 1D tubular CNSF fibers are closely connected with the adjacent ones (Fig. 1c), forming the continuous and interpenetrating 3D network. The TEM images (Fig. 1d and e) demonstrate that the sheet-like

silicate subunits are formed uniformly throughout the longitudinal axis of the tubular CNSF, which is consistent with the SEM observations. A high-resolution TEM (HR-TEM) examination (Fig. 1f) reveals that the 1D tubular CNSF is composed of ultrathin nanosheets of only $5 \pm 1 \text{ nm}$ in thickness, which might endow the structure with a high surface area. To further demonstrate the structural features of the as-prepared 1D tubular CNSF, the representative HAADF-STEM image and the corresponding elemental mapping further reveal the uniform distribution of C, Ni, and Si through the CNSF (Fig. S2†). All of the information available here has confirmed that the phyllosilicate nanosheets are intimately and uniformly incorporated into the 1D carbon framework. For comparison, bare nickel silicate (NSF) without carbon was prepared using neat silica fibers as starting materials. XRD patterns (Fig. 1g) verify the formation of nickel silicates, which can be assigned to the orthorhombic phases of $\text{Ni}_3\text{Si}_2\text{O}_5(\text{OH})_4$ (JCPDS no. 20-2791).²¹ The XRD pattern (Fig. 1g), SEM image (Fig. 1h and S3†) and HR-TEM image (Fig. 1i) indicate the similar crystalline structure and morphology of NSF to CNSF.

To further elucidate the elemental distributions of CNSF, energy-dispersive spectroscopy (EDS) and elemental mapping were performed which indicate the homogeneous distribution of Ni, Si, C and O in the sample (Fig. 2a and S4†). X-ray photoelectron spectroscopy (XPS) was performed to analyze the chemical and oxidation states of the CNSF (Fig. 2b and c). The wide scan spectra (Fig. 2b) confirmed that the CNSF sample contained only Ni, C, O and Si, and no other impurity elements were present. The binding energy of the Si 2p peaks was at $\sim 102.3 \text{ eV}$ (Fig. 2c), which suggested that the CNSF sample was silicate rather than composites of SiO_2 and metal oxides because the binding energy of Si 2p in silicates is 102–103 eV, whereas in SiO_2 it is higher ($\sim 103.5 \text{ eV}$).^{7,26} The

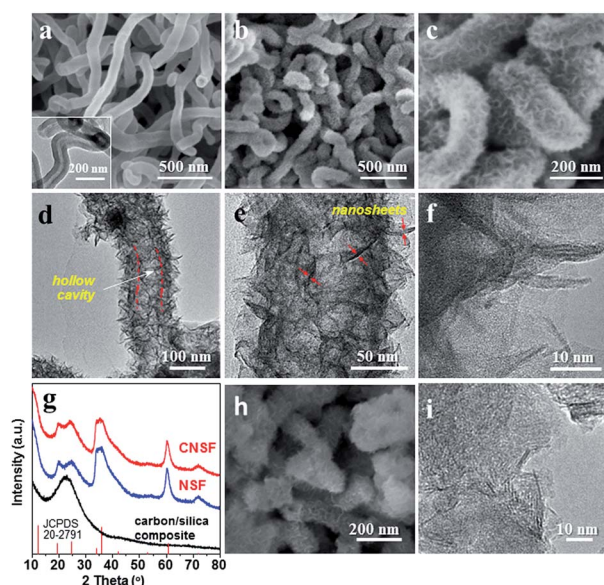


Fig. 1 (a) SEM image of the tubular carbon/silica composite substrate, where the inset shows the TEM image of the carbon/silica composite indicating the hollow structure. (b and c) SEM images of CNSF. (d and e) TEM images of CNSF. (f) HR-TEM image of CNSF. (g) XRD patterns of the carbon/silica composite, CNSF and bare nickel silicate samples (NSF). (h) SEM image of bare NSF. (i) HR-TEM image of bare NSF.

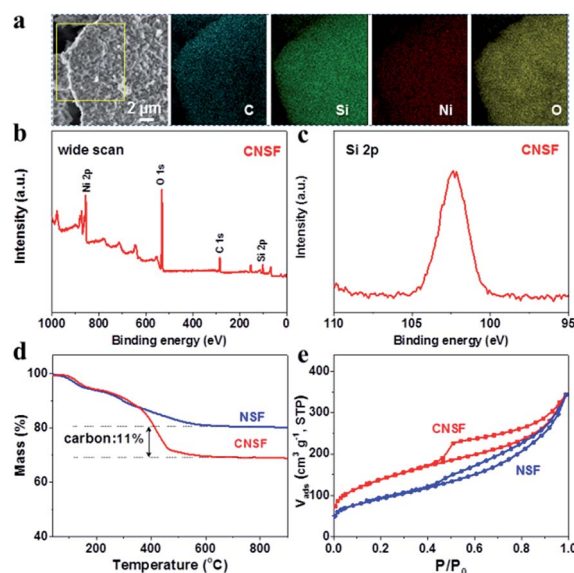


Fig. 2 (a) SEM image and EDS mapping of CNSF. XPS spectra of the CNSF: (b) wide-scan and (c) narrow-scan at the Si 2p region. (d) TG curves and (e) N_2 adsorption-desorption isotherms of CNSF and NSF.

thermogravimetric analysis (TGA, Fig. 2d) further demonstrates the existence of carbon in CNSF, and the amount is determined to be 11 wt%. A mass loss was observed below 200 °C in both CNSF and NSF, corresponding to the evaporation of adsorbed water.¹⁸ The weight loss at 200–500 °C is attributed to the loss of hydrated water and combustion of carbon in CNSF. N₂ adsorption–desorption measurements (Fig. 2e) indicate that the CNSF has a mesoporous structure with a high BET surface area of 489 m² g⁻¹ and V_{total} of 0.53 cm³ g⁻¹, providing abundant accessible pores for electrolyte diffusion during the electrochemical reaction process.

Such an integrated hierarchical architecture endows the carbon-incorporated nickel silicate nanosheet composite (CNSF) with great potential in lithium-storage applications. Fig. 3a shows the cyclic voltammetry (CV) curves of CNSF in the range of 0.01 V to 3 V at a scan rate of 0.2 mV s⁻¹. The initial cathodic sweep shows a broad peak at 0.7 V (vs. Li⁺/Li), which is assigned to the formation of a solid electrolyte interphase (SEI) layer,^{27–29} the lithium ion insertion into the crystalline lattice³⁰ and the reduction of the Ni²⁺.³¹ The subsequent cathodic peak appearing at around 1.6 V is characteristic of conversion-type electrochemical reactions with lithium, based on the reversible formation of lithium silicate (Li₄SiO₄)^{10,30,32} and possible formation of LiOH derived from OH⁻ ions in CNSF.³³ Regarding

the anodic sweep, the small feature at about 1.4 V might be related to the partially reversible SEI formation, and the peak at about 2.3 V is ascribed to the re-oxidation of the nickel. This observation is in good agreement with previous studies.^{30,31} Importantly, the subsequent CV curves strongly resemble that of the second cycle (Fig. 3a and S5[†]), indicating high electrochemical reversibility and good cycling stability of the CNSF electrode.³⁴

The charge–discharge profiles of the CNSF (Fig. 3b) and NSF (Fig. S6[†]) were conducted at a current density of 0.05 A g⁻¹ in the voltage window of 0.01–3.0 V. The CNSF presents a long voltage plateau at about 1.0 V, followed by a slope down to the cutoff voltage of 0.01 V during the first discharge cycle, which is in agreement with the CV results. From the above results, we deduce that the CNSF stores lithium through a conversion-type reaction mechanism based on the Ni(n)/Ni redox reaction and reversible formation of lithium silicate (Li₄SiO₄).^{10,29,30} Fig. 3b shows that CNSF delivers a high charge capacity of 1181 mA h g⁻¹ with an initial coulombic efficiency (CE) of 70.7% and nearly 100% in the subsequent cycles. The initial irreversible capacity loss could be attributed to the formation of the SEI layer and other irreversible processes such as the decomposition of electrolyte and the trapping of some lithium in the lattices, which is a common phenomenon amongst transition metal-based anode materials.^{35–38}

The cycling performance at 0.2 A g⁻¹ (Fig. 3c) of CNSF and NSF shows that CNSF keeps a stable reversible capacity of 889 mA h g⁻¹ after 60 cycles while the capacity of NSF decreased rapidly to 668 mA h g⁻¹, indicating that the carbon network can improve the electrical conductivity and structural integrity of CNSF which greatly contributes to the stable electrochemical performance. To reveal this, the impedance spectra of the CNSF and NSF are shown in Fig. 3d, where a distinctly smaller semicircle in the high-frequency region is observed for CNSF. The fitting results further demonstrate that the charge transfer resistance (R_2 , 70 Ω) of CNSF is smaller than that of bare NSF (130 Ω). The EIS results indicate that the built-in conductive carbon network improves the electronic conductivity, which is another underlying reason for the superior performance of CNSF over bare NSF.

The rate performances of CNSF and bare NSF were investigated by varying the current densities from 0.05 to 2.0 A g⁻¹ (Fig. 3e). The CNSF composite exhibits a much better rate performance than bare NSF. The specific reversible capacities of CNSF are 1145, 1107, 1017, 876, 813, 730, and 540 mA h g⁻¹ at current densities of 0.05, 0.1, 0.2, 0.5, 0.7, 1.0, and 2.0 A g⁻¹, respectively. When the current density returned to 0.2 A g⁻¹, a constant capacity of around 1045 mA h g⁻¹ was restored, indicating the structural stability of CNSF. The rate capability of the CNSF in this work also exceeds that of related nickel silicate samples reported previously, as indicated in Fig. 3f.^{10,17,18} To further demonstrate the advantages of such structures, two other silicates, manganese silicate and copper silicate, were synthesized and as shown in Fig. S7,[†] the two samples also show a stable cycling performance over 50 cycles at 0.5 A g⁻¹. This is strong evidence that the ultrathin phyllosilicate nanosheets with the incorporated conductive carbon greatly improve

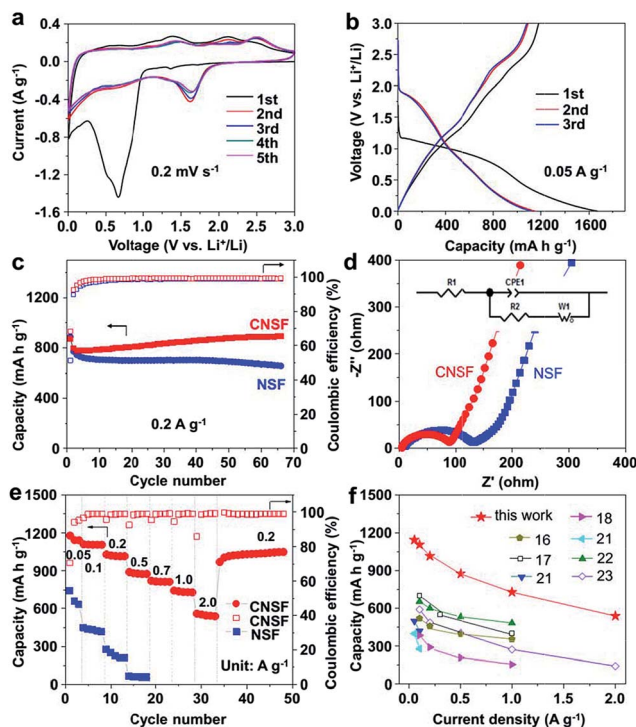


Fig. 3 (a) CV curves of the CNSF at a scan rate of 0.2 mV s⁻¹. (b) Discharge–charge profiles of the CNSF for the first three cycles at a current density of 0.05 A g⁻¹. (c) Cycling performance of CNSF at 0.2 A g⁻¹. (d) Nyquist plots of CNSF and NSF in a fresh coin cell used 12 h after assembly. (e) The rate capability of the CNSF hybrid and bare NSF. (f) The specific capacity of CNSF at various current densities, in comparison with that of previously reported nickel silicate based anode materials.

the electronic and ionic conductivity and the integrity of the electrode, and thus enable it to tolerate different charge and discharge currents.

To further demonstrate the suitability of this unique material design towards advanced LIB anodes, the long-life cycling performance of the CNSF composite was evaluated at a higher current density of 1.0 A g^{-1} (Fig. 4a). The capacity remains at 585 mA h g^{-1} after 200 cycles at 1.0 A g^{-1} , corresponding to a capacity retention of 98% (compared to the capacity of the 2nd cycle), demonstrating the excellent cyclability of CNSF. The electrochemical performance of the CNSF compares favorably with that of previously reported nickel silicates as shown in Table S2.† To further analyze the structural changes that occurred during the electrochemical test, SEM and EDX mapping analysis were used to observe the CNSF after 200 cycles (Fig. S8†), which displays that the overall morphology of the 1D fibers remained almost unchanged, indicating good mechanical stability and structural integrity of CNSF.

To measure the possibility for practical application in LIBs, the CNSF anode was assembled with the commercial cathode material of $\text{LiNi}_{1/3}\text{Co}_{1/3}\text{Mn}_{1/3}\text{O}_2$ (LiNCM) as a full battery. The LiNCM in the half cell delivers a stable capacity of 139 mA h g^{-1} at 0.1C ($1\text{C} = 278 \text{ mA g}^{-1}$) and good rate capability (103 mA h g^{-1} at 5C) as shown in Fig. S9.† The full cell delivered a high reversible capacity of 720 mA h g^{-1} based on the mass of anode material at 0.1 A g^{-1} , corresponding to 130 mA h g^{-1} based on the cathode material, with almost 100% capacity retention for 50 cycles (Fig. 4b and c). It is notable to mention that the high capacity nickel silicates (1107 mA h g^{-1} at 0.1 A g^{-1}) can greatly lighten the weight of anodes in full cell applications, equivalent to one third of the mass of graphite (theoretical capacity of 372 mA h g^{-1}). A fully charged CNSF//LiNCM full cell was employed to drive two commercial red light-emitting diodes (LEDs), each of which works at a voltage of 2.0 V (the inset of Fig. 4c and Video S1 in ESI†).

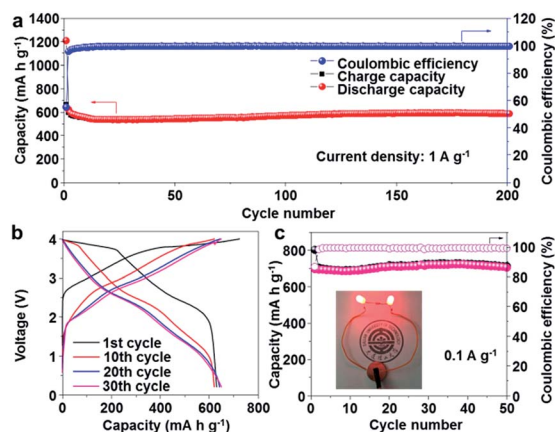


Fig. 4 (a) The cycling performance of the bare NSF and CNSF at a current density of 1.0 A g^{-1} . (b) Charge/discharge profiles of the CNSF//LiNCM full cell within a voltage window of 0.2–4.0 V at 0.1 A g^{-1} . (c) The cycling performance of the CNSF//LiNCM full cell at 0.1 A g^{-1} for 50 cycles. Inset: two commercial LEDs lighted by a coin-type CNSF//LiNCM full cell.

On the basis of the above results, the excellent electrochemical performance of the CNSF composite can be ascribed to the following aspects. Firstly, the incorporated conductive carbon affords highways for electrons transporting to the metal silicate, and meanwhile avoids the agglomeration of the ultrathin nanosheets. Secondly, the tubular nanostructures composed of ultrathin phyllosilicate nanosheets increase the electrode/electrolyte contact interface and are more favorable for providing sufficient electroactive sites. Also, the 1D hollow nanoarchitectures can accommodate the lithiation-induced strain and enhance the structural stability, rendering a stable cycling performance. Given the above, structural manipulation of silicate nanosheets and conductive carbon frameworks effectively integrates the advantages of both components, resulting in an outstanding lithium-storage performance.

4. Conclusion

A facile strategy for the preparation of ultrathin phyllosilicate nanosheets inlaid into carbon frameworks has been developed, derived from a tubular mesoporous carbon/silica composite substrate. The electrochemical investigation shows that the obtained hierarchical nanoarchitectures exhibit significantly enhanced lithium-storage properties under different testing conditions in comparison to the bare metal silicate counterparts, benefitting from the 1D hollow structure, ultrathin nanosheet units, and the incorporated conductive carbon. Such goal-directed structural manipulation of electroactive metal silicates with conductive carbon holds great potential in addressing the poor electrical conductivity and volume expansion issue of high capacity anode materials.

Conflicts of interest

There are no conflicts to declare.

Acknowledgements

This work was supported by the National Science Fund for the National Natural Science Foundation of China (No. 21376047 and No. 21473021), and Cheung Kong Scholars Programme of China (T2015036).

Notes and references

- 1 J. Cabana, L. Monconduit, D. Larcher and M. R. Palacin, *Adv. Mater.*, 2010, **22**, 170–192.
- 2 L. Yu, J. F. Yang and X. W. Lou, *Angew. Chem., Int. Ed.*, 2016, **55**, 13422–13426.
- 3 Z. Chen, M. Zhou, Y. Cao, X. Ai, H. Yang and J. Liu, *Adv. Energy Mater.*, 2012, **2**, 95–102.
- 4 R. Yi, J. Feng, D. Lv, M. L. Gordin, S. Chen, D. Choi and D. Wang, *Nano Energy*, 2013, **2**, 498–504.
- 5 H. J. Song, J.-C. Kim, M. Choi, C. Choi, M. A. Dar, C. W. Lee, S. Park and D.-W. Kim, *Electrochim. Acta*, 2015, **180**, 756–762.
- 6 Z. Gong and Y. Yang, *Energy Environ. Sci.*, 2011, **4**, 3223–3242.

- 7 C. Qiu, J. Jiang and L. Ai, *ACS Appl. Mater. Interfaces*, 2016, **8**, 945–951.
- 8 S.-M. Hao, J. Qu, Z.-S. Zhu, X.-Y. Zhang, Q.-Q. Wang and Z.-Z. Yu, *Adv. Funct. Mater.*, 2016, **26**, 7334–7342.
- 9 L. Liu, Y. Li, S. Yuan, M. Ge, M. Ren, C. Sun and Z. Zhou, *J. Phys. Chem. C*, 2010, **114**, 251–255.
- 10 W. Cheng, F. Rechberger, G. Ilari, H. Ma, W.-I. Lin and M. Niederberger, *Chem. Sci.*, 2015, **6**, 6908–6915.
- 11 Y. Yang, Q. Q. Liang, J. H. Li, Y. Zhuang, Y. H. He, B. Bai and X. Wang, *Nano Res.*, 2011, **4**, 882–890.
- 12 J. Qu, Y. Yan, Y. Yin, Y. Guo and W. Song, *ACS Appl. Mater. Interfaces*, 2013, **5**, 5777–5782.
- 13 Y. Yang, R. Jin, S. Song and Y. Xing, *Mater. Lett.*, 2013, **93**, 5–8.
- 14 Y. Sun, N. Liu and Y. Cui, *Nat. Energy*, 2016, 16071.
- 15 G. Chen, L. Yan, H. Luo and S. Guo, *Adv. Mater.*, 2016, **28**, 7580–7602.
- 16 X. Wei, C. Tang, X. Wang, L. Zhou, Q. Wei, M. Yan, J. Sheng, P. Hu, B. Wang and L. Mai, *ACS Appl. Mater. Interfaces*, 2015, **7**, 26572–26578.
- 17 S.-H. Yu, B. Quan, A. Jin, K.-S. Lee, S. H. Kang, K. Kang, Y. Piao and Y.-E. Sung, *ACS Appl. Mater. Interfaces*, 2015, **7**, 25725–25732.
- 18 C.-X. Gui, S.-M. Hao, Y. Liu, J. Qu, C. Yang, Y. Yu, Q.-Q. Wang and Z.-Z. Yu, *J. Mater. Chem. A*, 2015, **31**, 16551–16559.
- 19 T. Zhu, H. B. Wu, Y. Wang, R. Xu and X. W. Lou, *Adv. Energy Mater.*, 2012, **2**, 1497–1502.
- 20 N. Choudhary, C. Li, H.-S. Chung, J. Moore, J. Thomas and Y. Jung, *ACS Nano*, 2016, **10**, 10726–10735.
- 21 R. Jin, Y. Yang, Y. Li, X. Liu, Y. Xing, S. Song and Z. Shi, *Chem.–Eur. J.*, 2015, **21**, 9014–9017.
- 22 Q.-Q. Wang, J. Qu, Y. Liu, C.-X. Gui, S.-M. Hao, Y. Yu and Z.-Z. Yu, *Nanoscale*, 2015, **7**, 16805–16811.
- 23 C. Tang, J. Sheng, C. Xu, S. M. B. Khajehbashi, X. Wang, P. Hu, X. Wei, Q. Wei, L. Zhou and L. Mai, *J. Mater. Chem. A*, 2015, **3**, 19427–19432.
- 24 Y. Zhong, M. Yang, X. Zhou and Z. Zhou, *Mater. Horiz.*, 2015, **2**, 553–566.
- 25 X.-Q. Zhang, B. He, W.-C. Li and A.-H. Lu, *Nano Res.*, 2017, DOI: 10.1007/s12274-017-1737-6.
- 26 C. D. Wagner, D. E. Passoja, H. F. Hillery, T. G. Kinisky, H. A. Six, W. T. Jansen and A. J. Taylor, *J. Vac. Sci. Technol.*, 1982, **21**, 933–944.
- 27 C. B. Wang, L. W. Yin, D. Xiang and Y. X. Qi, *ACS Appl. Mater. Interfaces*, 2012, **4**, 1636–1642.
- 28 Z. Y. Cai, L. Xu, M. Y. Yan, C. H. Han, L. He, K. M. Hercule, C. J. Niu, Z. F. Yuan, W. W. Xu, L. B. Qu, K. N. Zhao and L. Q. Mai, *Nano Lett.*, 2015, **15**, 738–744.
- 29 M. M. Thackeray, W. I. F. David and J. B. Goodenough, *Mater. Res. Bull.*, 1982, **17**, 785–793.
- 30 F. Mueller, D. Bresser, N. Minderjahn, J. Kalhoff, S. Menne, S. Krueger, M. Winter and S. Passerini, *Dalton Trans.*, 2014, **43**, 15013–15021.
- 31 I. Elizabetha, A. K. Nair, B. P. Singh and S. Gopukumar, *Electrochim. Acta*, 2017, **230**, 98–105.
- 32 X. Sun, C. Yan, Y. Chen, W. Si, J. Deng, S. Oswald, L. Liu and O. G. Schmidt, *Adv. Energy Mater.*, 2014, **4**, 1300912.
- 33 L. Su, J. Hei, X. Wu, L. Wang and Z. Zhou, *Adv. Funct. Mater.*, 2017, 1605544.
- 34 Y. Xu, Y. Z. Li, S. Q. Liu, H. L. Li and Y. N. Liu, *J. Power Sources*, 2012, **220**, 103–107.
- 35 Q. Zhang, S. Ge, H. Xue, X. Wang, H. Sun and A. Li, *RSC Adv.*, 2014, **4**, 58260–58264.
- 36 Z. Y. Wang, Z. C. Wang, W. T. Liu, W. Xiao and X. W. Lou, *Energy Environ. Sci.*, 2013, **6**, 87–91.
- 37 T. Kim, Y. H. Mo, K. S. Nahm and S. M. Oh, *J. Power Sources*, 2006, **162**, 1275–1281.
- 38 K. Kang, K. Song, H. Heo, S. Yoo, G. S. Kim, G. Lee, Y. M. Kang and M. H. Jo, *Chem. Sci.*, 2011, **2**, 1090–1093.